Collisional excitation of HCNH(+) by He and H(2): New potential energy surfaces and inelastic rate coefficients

C T Bop, F Lique

Accepted to J. Chem. Phys. 10.1063/5.0141851

Collisional excitation of $HCNH^+$ by He and H_2: new potential energy surfaces and inelastic rate coefficients

C. T. Bop[1] and F. Lique[1]
Univ Rennes, CNRS, IPR (Institut de Physique de Rennes) - UMR 6251, F-35000 Rennes, France.

(*Electronic mail: cheikhtidiane.bop@ucad.edu.sn)

(Dated: 2 February 2023)

Protonated molecules have been increasingly detected in the interstellar medium (ISM) and usually astrochemical models fail at reproducing the abundances derived from observational spectra. Rigorous interpretation of detected interstellar emission lines requires prior calculations of collisional rate coefficients with H_2 and He, i.e. the most abundant species in the ISM. In this work, we focus on the excitation of $HCNH^+$ induced by collision with H_2 and He. Therefore, we first calculate *ab initio* potential energy surfaces (PESs) using the explicitly correlated and standard coupled cluster method with single, double, and non-iterative triple excitation in conjunction with the augmented-correlation consistent-polarized valence triple zeta basis set. Both the $HCNH^+-H_2$ and $HCNH^+-He$ potentials are characterized by deep global minima of 1426.60 cm^{-1} and 271.72 cm^{-1}, respectively and large anisotropies. From these PESs, we derive state-to-state inelastic cross sections for the 16 low-lying rotational energy levels of $HCNH^+$ using the quantum mechanical close-coupling approach. The differences between cross sections due to *ortho-* and *para*-H_2 impacts turn out to be minor. Using a thermal average of these data, we retrieve downward rate coefficients for kinetic temperatures of up to 100 K. As it could be anticipated, differences of up to two orders of magnitude exist between the rate coefficients induced by H_2 and He collisions. We expect that our new collision data will help to improve the disagreement between abundances retrieved form observational spectra and astrochemical models.

I. INTRODUCTION

Ion-neutral and neutral-neutral gas phase chemical reactions are thought to be the main formation routes for molecules in cold dense interstellar clouds.[1] Therefore, charged species are key intermediates in the enrichment of the chemical composition in these environments. However, only $\sim 10\%$ of the chemical species detected towards TMC-1, are positively charged. Indeed, due to their low abundances, the detection of these ions has turned out to be more difficult than that of the neutrals.

In recent years, a large number of protonated nitriles - HC_7NH^+,[2] HC_5NH^+,[3] HC_3NH^+,[4] HC_2NCH^+,[5] $NCCNH^+$,[6] and NC_4NH^+,[7] - has been detected in the interstellar medium (ISM). The simplest protonated nitrile, $HCNH^+$, was discovered in the ISM for the first time towards Sgr B2 through its $1 \rightarrow 0$, $2 \rightarrow 1$, and $3 \rightarrow 2$ rotational emission lines.[8] From the analysis of the spectra, the authors retrieved a fractional abundance with respect to hydrogen of 3×10^{-10}. Since then, $HCNH^+$ has been observed in numerous astronomical environments. In TMC-1 and DR 21(OH), the $HCNH^+$ abundance relative to hydrogen is as large as 1.9×10^{-9} and $\sim 10^{-10}$, respectively.[9–11]

The observations of protonated nitriles have been conducted successfully, thanks to the abundance of their neutral counterparts which have high proton affinities. Indeed, observational spectra as well as chemical models suggest that the $[MH^+]/[M]$ abundance ratio, between a protonated molecule (MH^+) and its neutral counterpart (M), increases with the increase of the proton affinity of M.[6] However, this trend does not seem to apply for the HC_nN ($n = 1, 3, 5, 7$) family. For instance, the proton affinity of HC_nN increases as a function of n (i.e. 712.9, 751.2, 770.0, 798.0 kJ mol^{-1}; see Refs.[2,12,13]) whereas the protonated-to-neutral abundance ratio observed in TMC-1 decreases with the increase of n (i.e. $\sim 6.0\times10^{-2}$, $\sim 4.3\times10^{-3}$, $\sim 4.2\times10^{-3}$, $\sim 2.6\times10^{-3}$; see Refs.[2,6]). This contradictory trend suggests to treat separately the chemistry regulating the $[HC_nNH^+]/[HC_nN]$ abundance ratio.

The protonated-to-neutral abundance ratio is sensitive to the ionization rate and thus to the physical conditions of the cloud.[6] Accordingly, constraining this ratio is crucial to better understand the chemistry of HC_nNH^+ and the physical conditions of the media where they are detected. Protonated nitriles are essentially produced by proton transfer from H_3^+ to the neutral and their destruction is caused by electrons via dissociative recombination.[14] Even though these reactions turn out to be the dominant processes and reasonably well-known at room temperature, chemical models still fail at accurately reproducing the observations. For example, using a cosmic ray ionization rate of 1.3×10^{-17} s^{-1}, a kinetic temperature of 10 K and a gas density of 2×10^4 cm^{-3} for TMC-1, the chemical model underestimates the observed $[HC_nNH^+]/[HC_nN]$ abundance ratio by a factor of $5-10$ (the larger discrepancy being recorded for $n = 1$).[2,6] These disagreements are usually thought to be originated from missing chemical reactions or inaccurate low temperature reaction rate constants in the chemical models. Another possibility that can explain the disagreement can originate from the simple approach that has been used for modelling the observations that could lead to inaccurate abundance of the protonated nitriles. It is of high interest to study the impact of non-local thermodynamic equilibrium (LTE) radiative transfer calculations (taking into account collisional data) on the determination of the observed abundances.

It has been shown in the literature that assuming LTE to interpret observational spectra tends to overestimate molecular

Accepted to J. Chem. Phys. 10.1063/5.0141851

abundances.[15–17] Indeed, the physical conditions of interstellar molecular clouds are in general such that the kinetic temperature differs from the excitation temperature of the lines. To accurately model this latter and derive molecular abundances from observational spectra, prior calculations of collisional rate coefficients are needed. Collisional excitation of HCN and HNC,[18–21] the neutral counterparts of $HCNH^+$, has been intensively investigated in the literature whereas the rotational energy transfer of $HCNH^+$ received less attention. To the best of our knowledge, the abundance of this cation has only been investigated under the LTE assumption. A possible consequence of this discrimination is to overestimate the observed abundance of $HCNH^+$ and thus the $[HCNH^+]/[HCN]$ ratio due to LTE-analysis.

The only scattering work dedicated to $HCNH^+$ so far, is its collisional excitation due to He.[22] State-of-the-art *ab initio* calculations were employed but the authors reported downward rate coefficients only for the 11 low-lying rotational levels. Helium has been considered as a reasonably good template for *para*-$H_2(j_2 = 0)$ since both species are spherical and contain two valence-electron. In fact, it is shown in the literature that using He-induced collisional rate coefficients instead of the actual data due to *para*-$H_2(j_2 = 0)$ impact is a bad approximation in the case of charged species since the scaling factor (a value of $2-4$) depends on the transition and the temperature.[23–25] Studying collisions between H_2 and $HCNH^+$ is then of high priority in order to accurately model observational spectra of this molecular cation. Hence, we investigate in this work the excitation of $HCNH^+$ due to collision H_2 using a new *ab initio* potential. In parallel, we also revisit the excitation of $HCNH^+$ by He in order to deeply compare the excitation of this cation by the two dominant colliders in the cold ISM.

The structure of this paper is as follows: the *ab initio* calculations are detailed in Section II, the results are presented and discussed in Section III and concluding remarks are given in Section IV.

II. COMPUTATIONAL DETAILS

A. Potential energy surface and analytical fit

The interaction potential between linear $HCNH^+(^1\Sigma^+)$ and $H_2(^1\Sigma_g^+)$/$He(^1S)$ is described using the rigid-rotor approximation. The H_2 bond length $<r_{H_2}>_0 = 0.767$ Å corresponds to the internuclear distance averaged over the ground vibrational wave function whereas the $r_{HC} = 1.0780$ Å, $r_{CN} = 1.1339$ Å and $r_{NH} = 1.0126$ Å, bond separations correspond to the $HCNH^+$ equilibrium geometry.[26,27] The use of equilibrium geometry in polyatomic molecules is quite usual since the vibrational wave functions are not always available. In this work, we investigate the $HCNH^+-H_2$ four dimensional potential energy surface (4D PES) for the first time employing the Jacobi coordinate system (as shown in Fig.1). R stands for the distance between the centers of mass of the two monomers, the angle θ_1 (θ_2) describes the orientation of $HCNH^+$ (H_2) with respect to the colliding axis and ϕ is the dihedral angle between the half-planes containing $HCNH^+$ and H_2. The definition of R and θ_1 is also valid for the $HCNH^+-He$ potential (2D PES).

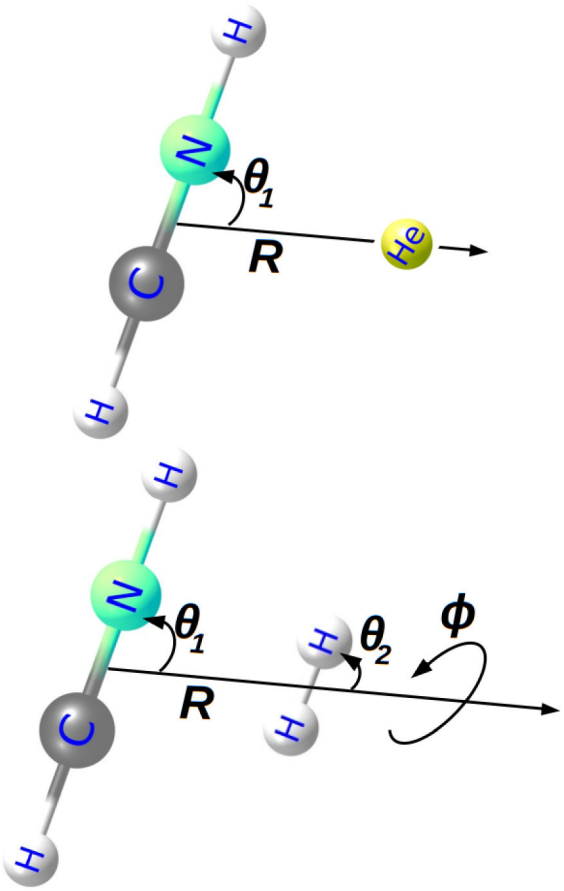

FIG. 1. Jacobi coordinate system for the $HCNH^+-H_2$ and $HCNH^+-He$ van der Waals complexes.

As we aim to compare the data obtained using He and H_2 as projectiles, we compute a new $HCNH^+-He$ 2D PES to avoid any bias due to the level of theory used in the PES construction. Indeed, Nkem et al.[22] employed the standard coupled cluster method with single, double, and non-iterative triple excitation [CCSD(T)][28,29] along with the augmented-correlation consistent-polarized valence triple zeta basis set (aug-cc-pVTZ)[30] and mid-bond functions to describe the PES whereas we introduce the explicit treatment of the electron correlation [CCSD(T)-F12][31] and ignore the mid-bond functions. The practical accuracy of the computed quantities approaches that of CCSD(T) in conjunction with a complete basis set.[31] Therefore, we use the same level of theory to compute both the 2D and 4D PESs.

For all electronic calculations, we use the `MOLPRO` quantum chemistry package version 2015.[32,33] For both collisional systems, the PESs are generated using 45 R-grid points (from 4.50 to 20 a_0) and 15-point Gauss-Legendre quadrature for θ_1. Additionally, 9-point Gauss-Chebyshev (for ϕ) and 5-point Gauss-Legendre (for θ_2) quadrature are used in the 4D PES

to describe the rotational motion of H_2. The size consistency error due to the CCSD(T)-F12 method is corrected for all geometries by subtracting the potential obtained at $R = 200\ a_0$

$$V(R,\alpha) = V(R,\alpha) - V(R = 200\ a_0, \alpha), \quad (1)$$

where α stands for $\{\theta_1, \theta_2, \phi\}$ for the 4D PES and θ_1 for the 2D PES. To take into account the ionic nature of the collional systems, we calculate the PESs from $R = 20\ a_0$ up to $R = 60\ a_0$ using the standard CCSD(T) method since CCSD(T)-F12 does not always describe correctly the long-range interaction. For both the $HCNH^+-H_2$ and $HCNH^+-He$ systems, the potential energies calculated with the two level of theories differ by less than 3% at $R = 20\ a_0$. Therefore, the two sets of data [$V(R \leq 20\ a_0, \alpha)$ and $V(R \geq 21\ a_0, \alpha)$] are smoothly connected using cubic spline routine. For all *ab initio* points, the errors due to basis set superposition are corrected using the counterpoise method,[34]

$$V(R,\alpha) = E_{HCNH^+-A}(R,\alpha) - E_{HCNH^+}(R,\alpha) - E_A(R,\alpha), \quad (2)$$

where A stands for H_2 for the 4D PES and He for the 2D PES.

To derive analytical representation of the $HCNH^+-H_2$ *ab initio* PES we use contracted normalized bispherical harmonics (Eq. 3) as follows:

$$V(R,\theta_1,\theta_2,\phi) = \sum_{L_1 L_2 L} v_{L_1 L_2 L}(R) A_{L_1 L_2 L}(\theta_1,\theta_2,\phi). \quad (3)$$

Eq. 4 introduces the definition of the bispherical harmonics,

$$A_{L_1 L_2 L}(\theta_1,\theta_2,\phi) = \sqrt{\frac{2L_1+1}{4\pi}} \Big[\begin{pmatrix} L_1 & L_2 & L \\ 0 & 0 & 0 \end{pmatrix} \times P_{L_1 0}(\theta_1) \times P_{L_2 0}(\theta_2) + 2 \sum_{M=1}^{\min(L_1,L_2)} \begin{pmatrix} L_1 & L_2 & L \\ M & -M & 0 \end{pmatrix} \times P_{L_1 M}(\theta_1) P_{L_2 M}(\theta_2) cos(M\phi) \Big]. \quad (4)$$

L_1 and L_2 stand for the rotational motion of $HCNH^+$ and H_2, respectively. They vary up to $L_{1max} = 14$ and $L_{2max} = 4$, respectively. By definition, $L = |L_1 - L_2|, ..., L_1 + L_2$ and L_2 takes only even values due to the symmetry of H_2. The root-mean-square error (rmse) generated by the analytical fit (Eq. 3) is $\sim$12 cm^{-1} at $R = 4.50\ a_0$ but it quickly drops down to less than 1 cm^{-1} at $R = 5.5\ a_0$ and few [$10^{-5} - 10^{-2}$] cm^{-1} above 8 a_0. It is worth noting that in the region where the rmse is greater than 1 cm^{-1}, the absolute value of the potential is larger than 300 cm^{-1}.

Concerning the $HCNH^+-He$ *ab initio* PES, Legendre polynomials [$P_{L_1}(\theta_1)$] are employed to determine the analytical expression,

$$V(R,\theta_1) = \sum_{L_1}^{L_{1max}} v_{L_1}(R) P_{L_1}(\theta_1), \quad (5)$$

where L_1 and L_{1max} are exactly as defined above. This expansion reproduces the *ab initio* data with relative errors less than 1%.

Let us notice that the `MOSLCAT` built-in `POTENL` routine extrapolates the radial coefficients $v_\lambda(R)$ according to the following inverse exponent,[35] to generate the potentials for radial distances larger the 60 a_0, i.e. beyond the *ab initio* calculations.

$$v_\lambda(R) = \frac{C_\lambda}{R^{\eta_\lambda}} \quad (6)$$

Here, v_λ stands for v_{L_1} and $v_{L_1 L_2 L}$ for the 2D and 4D potentials, respectively and the coefficients C_λ and η_λ are calculated using the last two values of v_λ.

B. Cross sections and rate coefficients

The dynamical processes we are investigating are summarized by Eq. 7. The projectile A stands for *para*-$H_2(j_2 = 0)$ and He. We note by j_1 and j_2 the rotational quantum numbers of $HCNH^+$ and H_2, respectively.

$$HCNH^+(j_1) + A \rightarrow HCNH^+(j_1') + A \quad (7)$$

State-to-state inelastic cross sections (σ) involving the 16 low-lying rotational energy levels of $HCNH^+$ ($j_1 = 0 - 15$) are calculated in the [2.5 – 800.0] cm^{-1} total energy range. In order to correctly describe the resonances, we scan the energy range using a fine step of 0.1 cm^{-1} up to 400 cm^{-1} (i.e up to $\sim$ 100 cm^{-1} above the $HCNH^+$ rotational energy level $j_1 = 15$). For higher total energies, we smoothly increase the step size up to 10 cm^{-1}.

The close-coupling quantum mechanical approach implemented in the `MOLSCAT` computer code,[35–37] supplemented with the log derivative-airy integrator,[38] is used to solve the coupled equations and derive state-to-state inelastic cross sections. Convergence calculations are carried out first to determine the parameters necessary for the propagator. We set the $HCNH^+$ rotational basis large enough including j_1 up to 30, i.e. all energy levels of interest along with at least 6 channels above.

For the $HCNH^+-H_2$ collisional system, the *para*-H_2 (*ortho*-H_2) rotational manifold includes only $j_2 = 0$ ($j_2 = 1$) in the calculations. The contribution from upper energy levels (i.e. $j_2 = 2$ and $j_2 = 3$) is checked by comparing partial cross sections summed over total angular momenta up to $J = 10$, for example $\sigma(j_2 = 0)$ versus $\sigma(j_2 = 0 - 2)$. Indeed, the inclusion of $j_2 = 0 - 2$ and $j_2 = 1 - 3$ respectively in the *para*-H_2 and *ortho*-H_2 rotational bases leads to a mean deviation of $\sim$ 20% considering all transitions but it also increases the computational time by a factor of $\sim$ 100. Let us notice that, such relative errors are not expected to have significant impact in radiative transfer calculations.

The STEPS-parameter which is inversely proportional to the kinetic energy (E_k) is decreased (from 50 to 10) with the increase of the energy to keep the integration step below 0.2 a_0. The rotational energy levels are calculated using the spectroscopic constants of $HCNH^+$ [$B_0 = 1.2360$ cm^{-1} and $D_0 = 1.6075 \times 10^{-6}$ cm^{-1}] and H_2 [$B_0 = 59.322$ cm^{-1} and $D_0 = 0.047$ cm^{-1}].[26,39]

Accepted to J. Chem. Phys. 10.1063/5.0141851

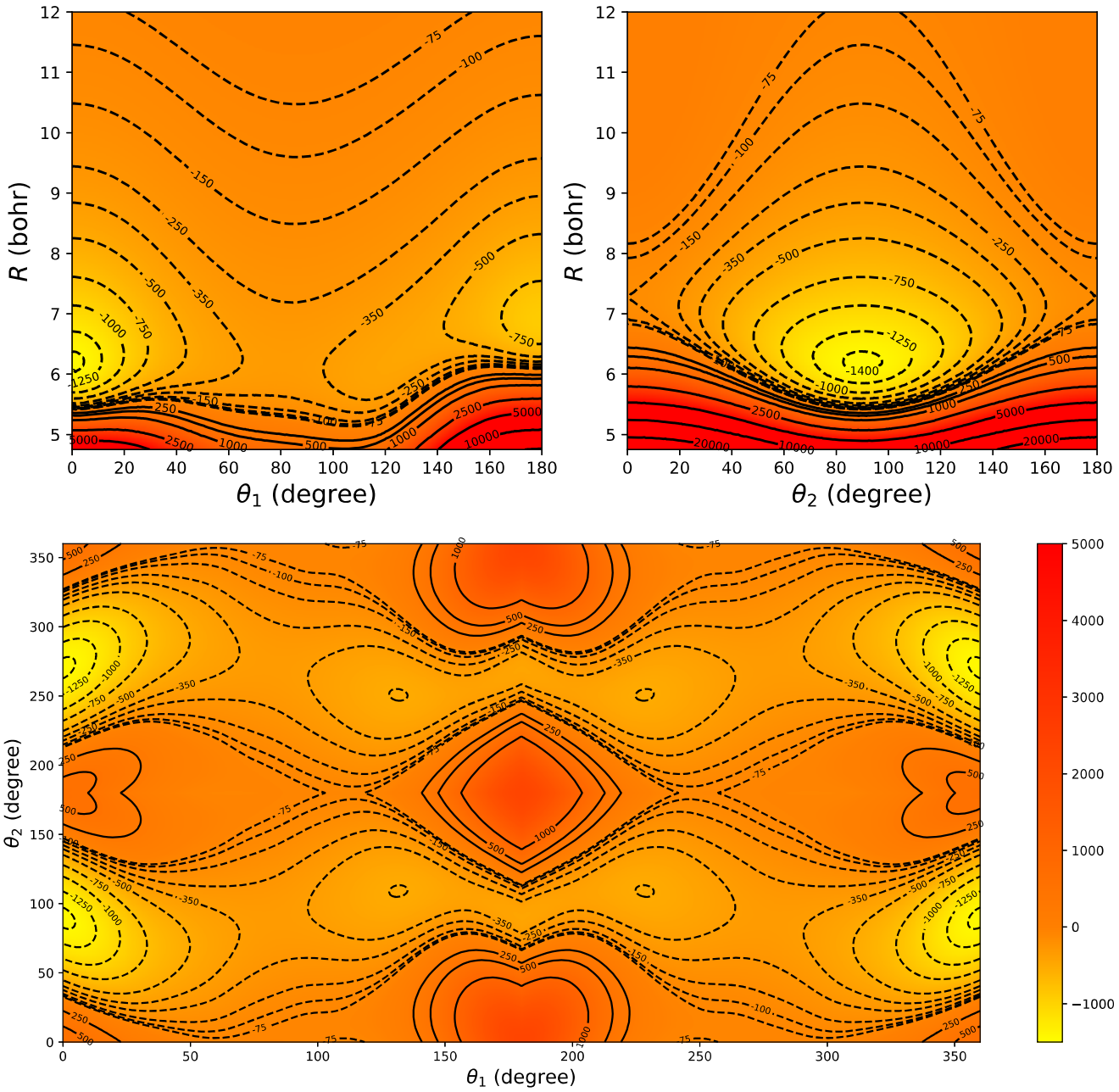

FIG. 2. Contour plots of bi-dimensional cuts of the $HCNH^+-H_2$ 4D PES. For the upper panels, $\{\theta_2,\phi\} = \{90^\circ, 0^\circ\}$ at the left-hand side and $\{\theta_1,\phi\} = \{0^\circ, 0^\circ\}$ at the right-hand side and for the lower panel, $\{\phi, R\} = \{0^\circ, 6.25\ a_0\}$. The color map scale (lower panel) and the contours show the interaction potential in cm^{-1} for all panels. The fixed parameters stand for the coordinates of the global minimum.

By mean of a thermal average of the cross sections over the Maxwell-Boltzmann kinetic energy distribution, we derive collisional rate coefficients (k) up to a kinetic temprature (T) of 100 K,

$$k_{j_1\to j_1'}(T) = \left(\frac{8}{\pi\mu\beta}\right)^{1/2}\beta^2\int_0^\infty E_k\sigma_{j_1\to j_1'}(E_k)e^{-\beta E_k}\,dE_k \quad (8)$$

where $\mu = 1.8075$ au (3.5024 au) stands for the reduced mass of the $HCNH^+-H_2$ ($HCNH^+-He$) collisional system and $\beta = (k_B T)^{-1}$.

III. RESULTS

We show in Fig. 2 contour plots of bi-dimensional cuts of the $HCNH^+-H_2$ 4D PES. For each panel, the fixed pa-

Accepted to J. Chem. Phys. 10.1063/5.0141851

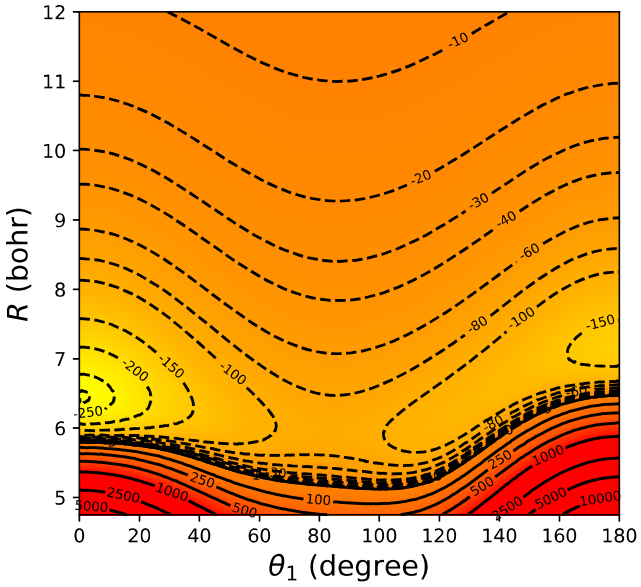

FIG. 3. Contour plots of the $HCNH^+-He$ PES as a function of R and θ_1. The contours show the interaction potential in cm^{-1}.

TABLE I. Comparison of the global minima (in unit of cm^{-1}) of the 2D and 4D PESs of $HCNH^+-He$ and $HCNH^+-H_2$, respectively.

R (a_0)	θ_1 (degree)	$HCNH^+-He$		$HCNH^+-H_2$
6.50	0	266.90[a]	271.72	–
6.25	0	–	–	1426.60

[a] refers to Nkem et al.[22]

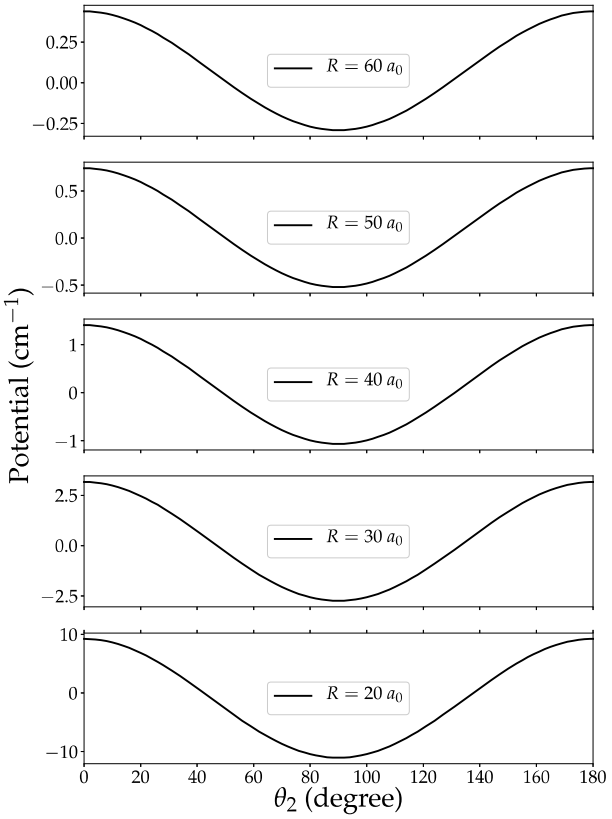

FIG. 4. Long-range interaction energy (in cm^{-1}) of the $HCNH^+-H_2$ complex as a function of R and θ_2, for $\theta_1 = \phi = 0°$.

rameters correspond to the coordinates of the global minimum ($\theta_1 = 0°$, $\theta_2 = 90°$ and $R = 6.25$ a_0 with ΔE = -1426.60 cm^{-1}). Let us notice that the interaction potential is not sensitive to ϕ in the T-shape configuration of the complex, i.e. $\theta_1 = 0°$ and $\theta_2 = 90°$. In general, the anisotropy of the potential with respect to ϕ is very weak (see appendix A).

Regarding θ_1 and θ_2, the interaction between $HCNH^+$ and H_2 is very anisotropic as one can see from Fig. 2. $V(R, \theta_1, \theta_2 = 90°, \phi = 0°)$ presents two minima at the T-shape configurations ($\theta_1 = \{0°, 180°\}$) and the shallower (ΔE = -887.34 cm^{-1} obtained at $R = 7.0$ a_0) corresponds to the side-on approach of H_2 towards the CH-end of $HCNH^+$ (i.e. $\theta_1 = 180°$). Due to the quasi-symmetric shape of $HCNH^+$, the potential is nearly symmetric with respect to θ_1 especially for $R \geq 8$ a_0.

Concerning $V(R, \theta_2, \theta_1 = 0°, \phi = 0°)$, the interaction is symmetric at $\theta_2 = 90°$ due to the homonuclearity of H_2. The lower panel better highlights the anisotropy of the interaction which persists even in the repulsive region. The global minimum mentioned above is also observed here whereas the secondary minimum, ΔE -503.03 cm^{-1}, occurs at $\{\theta_1, \theta_2\}$ = $\{132°, 109°\}$ due to the change of R from 7 a_0 to 6.25 a_0.

Fig. 3 displays the dependence on θ_1 and R of the $HCNH^+-He$ interaction potential. The newly computed PES is very similar in shape (including the position of the minima) and magnitude to that of Nkem et al.[22] The new 2D PES presents a global minimum of 271.72 cm^{-1} which is 5 cm^{-1} deeper than the previous calculations. Apart from the strength of the interaction, the 2D PES is very similar to the $V(R, \theta_1, \theta_2 = 90°, \phi = 0°)$ bi-dimensional cut of the 4D PES. Table I shows a comparison of the global minima and their positions. As one can see, the minima of the 2D PESs are located at the same $HCNH^+$ orientations but they are ~ 5 times shallower than the minimum of the 4D PES which corresponds to the side-on approach of H_2.

Fig.4 depicts the long-range interaction of the $HCNH^+-H_2$ complex as a function of θ_2. The potential is highly sensitive to the rotation of H_2 for radial distances of up to 50 a_0 where the amplitude varies by about 1 cm^{-1}. Indeed, this finding is not surprising since at the long-range, the potential potential is dominated by the charge-quadrupole interaction which is sensitive the rotation of H_2 (i.e. the quadrupole) and slowly drops as R^{-3}. This behaviour clearly justifies the extension of our *ab initio* calculations up to 60 a_0 where the amplitude change of the interaction decreases down to 0.5 cm^{-1}.

We show in Fig. 5 the dependence on kinetic energy of state-to-state inelastic cross sections of $HCNH^+$ induced by collision with *para*-H_2 and He. For both collisional systems, the cross sections behave similarly presenting several resonances (shape and Feshbach type) and an amplitude

Accepted to J. Chem. Phys. 10.1063/5.0141851

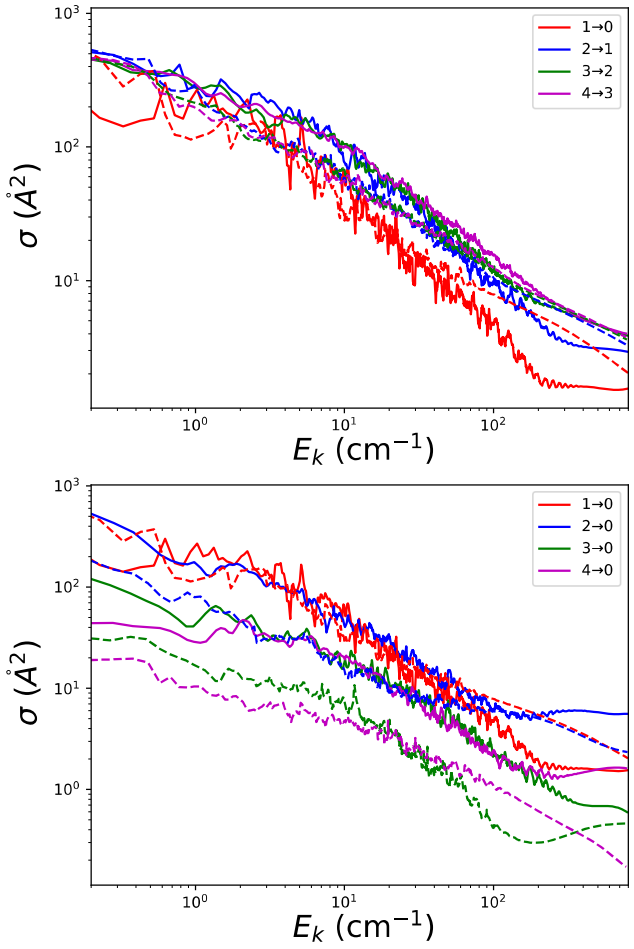

FIG. 5. Kinetic energy dependence of state-state inelastic cross sections of $HCNH^+$ induced by collision with *para*-$H_2(j_2 = 0)$ and He for selected downward transitions. The solid and dashed lines stand for the *para*-H_2 and He-induced cross sections, respectively.

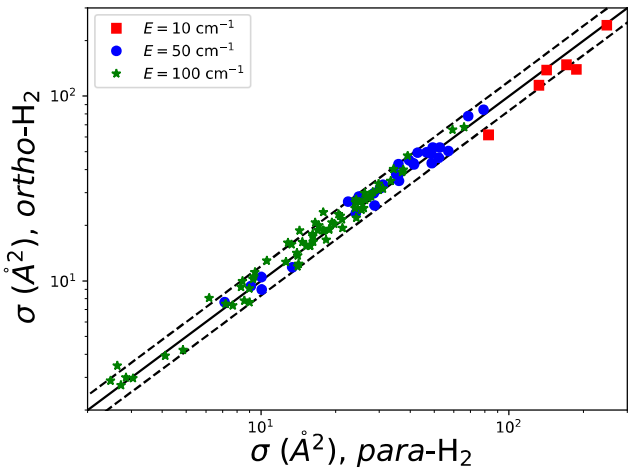

FIG. 6. Comparison of the $HCNH^+$ cross sections induced by collision with *ortho*-$H_2(j_2 = 1)$ and *para*-$H_2(j_2 = 0)$ projectiles for selected total energies. To keep the same kinetic energy for both collisional systems, we set the rotational energy of $H_2(j_2 = 1)$ to zero. The solid diagonal line stands for $y = x$ and the dashed lines delimit the region where the difference is less than a factor of 1.2.

that quickly drops with the increase of the kinetic energy-logarithm. Therefore, as for typical ion-molecule collisional cross sections, our calculations exhibit the Langevin behaviour. A global analysis of Fig. 5 shows that the lower panel, where $\Delta j_1 \geq 1$, better highlights the difference between the *para*-H_2 and He-induced cross sections than the upper panel for which $\Delta j_1 = 1$.

Concerning the H_2 nuclear spin symmetries, we compare in Fig. 6 the $HCNH^+$ cross sections due to both *ortho*-$H_2(j_2 = 1)$ and *para*-$H_2(j_2 = 0)$ collisions. Slight differences (i.e. less than a factor of 1.2 with few exceptions) exist between the two sets of data. This is a typical feature of cross sections induced by collision between molecular ions and H_2, as shown in detail in previous works.[40,41] This finding supplemented with the low population of *ortho*-H_2 in cold astrophysical environments, i.e. the regions we are interested in, let us not to calculate collisional rate coefficients of $HCNH^+$ by *ortho*-H_2 in this work. Nevertheless, these data can be inferred from the *para*-$H_2(j_2 = 0)$ collisional rate coefficients, if needed.

We display in Fig. 7 the dependence on Δj_1 of the $HCNH^+$ downward rate coefficients induced by collisions with *para*-H_2 and He for selected temperatures. For the (H_2) He-induced rate coefficients, the (upper) lower panel shows a dominance of the ($\Delta j_1 = 2$) $\Delta j_1 = 1$ transition. Nevertheless, there is no clear propensity rules in favor of (even) odd Δj_1 transitions for the (H_2) He-induced collisional data. This lack of clear propensity rule can be related to the features of the PESs. Indeed, the quasi-symmetric shape of the interaction potentials fosters even Δj_1 transitions whereas the anisotropy strengthens odd Δj_1 transitions.

The comparison between the new $HCNH^+$-He rate coefficients and those computed by Nkem et al.,[22] reveals slight differences which appear only at low temperature (see the lower panel of Fig. 7). This finding is not surprising since both PESs are very similar and present a difference of only ~ 5 cm^{-1} for the global minimum.

A simultaneous look at both panels shows an increasing dominance with the increase of Δj_1 in favor of rate coefficients induced by collision with *para*-H_2. For instance, the two sets of data differ by a factor of ~ 2 for $\Delta j_1 = 1$, 10 for $\Delta j_1 = 5$ and 100 for $\Delta j_1 = 10$. These disagreements are related to the $HCNH^+-He$ and $HCNH^+-H_2$ PESs which are quite different as discussed in detail in the beginning of this section. In summary, He is a bad template for *para*-H_2 in the collisional excitation of $HCNH^+$. However, it is worth mentioning that the He-induced rate coefficients computed in this work are not useless since the abundance of this species in the ISM is about 10% of the gas density. For example, Agúndez et al. adopted a He abundance relative to H_2 of 0.17 in non-LTE analysis of the $HCCNCH^+$ observational spectra.[5]

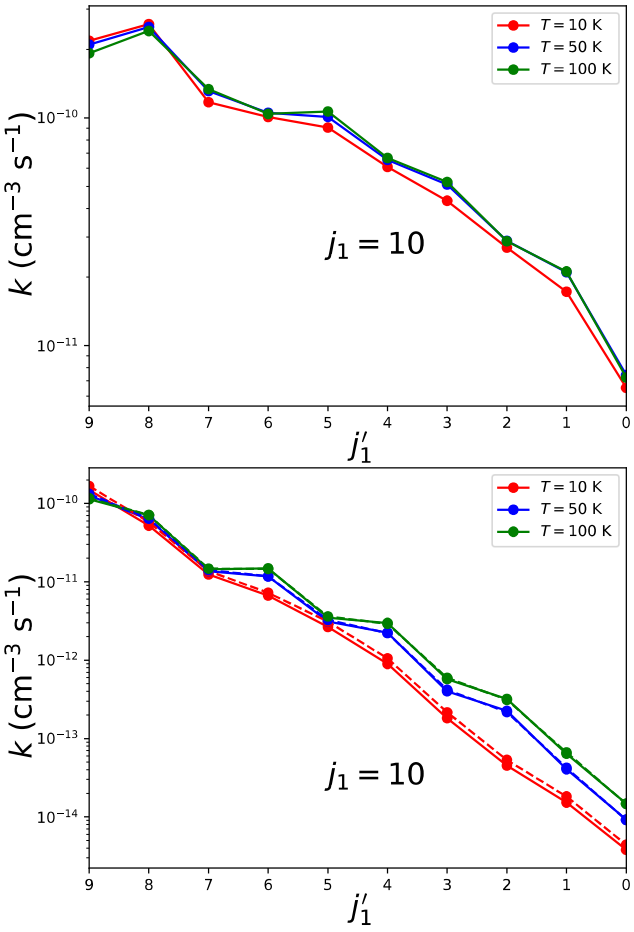

FIG. 7. Propensity rules for the downward rate coefficient of $HCNH^+$ induced by collision with *para*-H_2 (upper panel) and He (lower panel) for selected temperatures. The dashed lines stand for $HCNH^+$-He rate coefficients computed by Nkem et al.[22]

IV. CONCLUSION

The first 4D PES of the $HCNH^+-H_2$ collisional system is computed using the CCSD(T)-F12/aug-cc-pVTZ level of theory and the long-range interaction is described by mean of the standard CCSD(T)/aug-cc-pVTZ. A new 2D PES for the $HCNH^+$-He interaction is also calculated using the same level of theory. State-to-state inelastic cross sections of $HCNH^+$ induced by collision with both He and and *para*-$H_2(j_2 = 0)$ are retrieved, for total energies of up to 800 cm^{-1}, using the close-coupling quantum mechanical approach. By thermally averaging these cross sections, we determine rate coefficients for rotational transitions between the 16 low-lying energy levels of $HCNH^+$ for temperatures of up to 100 K.

Both interaction potentials (2D and 4D) exhibit large anisotropies with respect to the $HCNH^+$ rotation and two minima corresponding to linear approaches towards the H-ends. The global minimum is observed for the projectile approach (H_2 side-on approach for the 4D PES) towards the CH-end. A comparison of $HCNH^+$ collisional cross sections induced by *ortho*-$H_2(j_2 = 1)$ and *para*-$H_2(j_2 = 0)$ confirms the low influence of the H_2 symmetries in collisional excitation of molecular ions mentioned in the literature. Typically, we obtain differences less than a factor of 1.2. On the other hand, comparing *para*-H_2 and He-induced rate coefficients reveals differences ranging from a factor of 2 (for low Δj_1 transitions) to a factor of 100 (for large Δj_1 transitions) depending on the transitions. Therefore, we confirm that He is a bad template for *para*-$H_2(j_2 = 0)$ for the excitation of molecular ions.

The collisional rate coefficients presented in this paper, supplemented with the $HCN-H_2$ and $HNC-H_2$ collisional data,[42] will likely play a key role in the constraint of the $[HCNH^+]/[HCN + HNC]$ abundance ratio observed in cold dense molecular clouds and accordingly the cosmic ray ionization rate. Hyperfine resolved collisional rate coefficients and the impact of isotopic substitution in the excitation of $HCNH^+$ will be presented in a forthcoming paper.

CONFLICTS OF INTEREST

There are no conflicts of interest to declare.

SUPPLEMENTARY MATERIAL

A Fortran routine for generating the potential is available as supplementary material.

DATA AVAILABILITY

The data underlying this manuscript are available from the corresponding author upon reasonable request.

ACKNOWLEDGEMENTS

The authors acknowledge the European Research Council (ERC) for funding the COLLEXISM project No 811363, the Programme National "Physique et Chimie du Milieu Interstellaire" (PCMI) of Centre National de la Recherche Scientifique (CNRS)/Institut National des Sciences de l'Univers (INSU) with Institut de Chimie (INC)/Institut de Physique (INP) co-funded by Commissariat a l'Energie Atomique (CEA) and Centre National d'Etudes Spatiales (CNES). F.L. acknowledges the Institut Universitaire de France.

[1] M. Agúndez and V. Wakelam, Chemical Reviews **113**, 8710–8737 (2013).
[2] C. Cabezas, M. Agúndez, N. Marcelino, B. Tercero, R. Fuentetaja, P. de Vicente, and J. Cernicharo, Astronomy & Astrophysics **659**, L8 (2022).
[3] N. Marcelino, M. Agúndez, B. Tercero, C. Cabezas, C. Bermúdez, J. Gallego, P. Devicente, and J. Cernicharo, Astronomy & Astrophysics **643**, L6 (2020).
[4] K. Kawaguchi, Y. Kasai, S.-I. Ishikawa, M. Ohishi, N. Kaifu, and T. Amano, "Detection of a new molecular ion hc3nh (+) in tmc-1," The Astrophysical Journal **420**, L95–L97 (1994).
[5] M. Agúndez, C. Cabezas, N. Marcelino, R. Fuentetaja, B. Tercero, P. de Vicente, and J. Cernicharo, Astronomy & Astrophysics **659**, L9 (2022).

[6]Agúndez, M., Cernicharo, J., de Vicente, P., Marcelino, N., Roueff, E., Fuente, A., Gerin, M., Guélin, M., Albo, C., Barcia, A., Barbas, L., Bolaño, R., Colomer, F., Diez, M. C., Gallego, J. D., Gómez-González, J., López-Fernández, I., López-Fernández, J. A., López-Pérez, J. A., Malo, I., Serna, J. M., and Tercero, F., A&A **579**, L10 (2015).
[7]M. Agúndez, C. Cabezas, N. Marcelino, R. Fuentetaja, B. Tercero, P. de Vicente, and J. Cernicharo, Astronomy & Astrophysics **669**, L1 (2023).
[8]L. Ziurys and B. Turner, The Astrophysical Journal **302**, L31–L36 (1986).
[9]P. Schilke, C. Walmsley, T. Millar, and C. Henkel, Astronomy and Astrophysics **247**, 487–496 (1991).
[10]L. Ziurys, A. Apponi, and J. Yoder, The Astrophysical Journal **397**, L123–L126 (1992).
[11]T. Hezareh, M. Houde, C. McCoey, C. Vastel, and R. Peng, The Astrophysical Journal **684**, 1221 (2008).
[12]E. P. Hunter and S. G. Lias, Journal of Physical and Chemical Reference Data **27**, 413–656 (1998).
[13]S. J. Edwards, C. G. Freeman, and M. J. McEwan, International Journal of Mass Spectrometry **279**, 82–86 (2009).
[14]V. Wakelam, E. Herbst, J.-C. Loison, I. Smith, V. Chandrasekaran, B. Pavone, N. Adams, M.-C. Bacchus-Montabonel, A. Bergeat, K. Béroff, *et al.*, The Astrophysical Journal Supplement Series **199**, 21 (2012).
[15]J. Cernicharo, B. Lefloch, M. Agúndez, S. Bailleux, L. Margulès, E. Roueff, R. Bachiller, N. Marcelino, B. Tercero, C. Vastel, *et al.*, The Astrophysical journal letters **853**, L22 (2018).
[16]D. Ndaw, C. T. Bop, G. Dieye, N. B. Faye, and F. Lique, Monthly Notices of the Royal Astronomical Society **503**, 5976–5983 (2021).
[17]C. T. Bop, F. Lique, A. Faure, E. Quintas-Sánchez, and R. Dawes, Monthly Notices of the Royal Astronomical Society **501**, 1911–1919 (2020), https://academic.oup.com/mnras/article-pdf/501/2/1911/35335662/staa3821.pdf.
[18]E. Sarrasin, D. B. Abdallah, M. Wernli, A. Faure, J. Cernicharo, and F. Lique, Monthly Notices of the Royal Astronomical Society **404**, 518–526 (2010).
[19]F. Dumouchel, J. Kłos, and F. Lique, Physical Chemistry Chemical Physics **13**, 8204–8212 (2011).
[20]D. Ben Abdallah, F. Najar, N. Jaidane, F. Dumouchel, and F. Lique, Monthly Notices of the Royal Astronomical Society **419**, 2441–2447 (2012).
[21]M. H. Vera, Y. Kalugina, O. Denis-Alpizar, T. Stoecklin, and F. Lique, The Journal of Chemical Physics **140**, 224302 (2014).
[22]C. Nkem, K. Hammami, I. Y. Halalaw, L. C. Owono Owono, and N.-E. Jaidane, Astrophysics and Space Science **349**, 171–179 (2014).
[23]T. Monteiro, Monthly Notices of the Royal Astronomical Society **214**, 419–427 (1985).
[24]K. M. Walker, F. Lique, F. Dumouchel, and R. Dawes, Monthly Notices of the Royal Astronomical Society **466**, 831–837 (2017).
[25]C. T. Bop, Monthly Notices of the Royal Astronomical Society **487**, 5685–5691 (2019).
[26]K. Huber, (Springer US, 2013).
[27]P. Botschwina, A. Heyl, M. Horn, and J. Flugge, Journal of Molecular Spectroscopy **163**, 127–137 (1994).
[28]P. J. Knowles, C. Hampel, and H.-J. Werner, The Journal of chemical physics **99**, 5219–5227 (1993).
[29]P. J. Knowles, C. Hampel, and H.-J. Werner, The Journal of Chemical Physics **112**, 3106–3107 (2000).
[30]T. H. Dunning Jr, The Journal of chemical physics **90**, 1007–1023 (1989).
[31]G. Knizia, T. B. Adler, and H.-J. Werner, The Journal of chemical physics **130**, 054104 (2009).
[32]H. Werner, P. Knowles, G. Knizia, F. Manby, and M. Schütz, "Wiley interdiscip," Rev.: Comput. Mol. Sci **2**, 242–253 (2012).
[33]H. Werner, P. Knowles, G. Knizia, F. Manby, M. Schütz, P. Celani, W. Györffy, D. Kats, T. Korona, R. Lindh, *et al.*, See http://www. molpro. net (2015).
[34]S. F. Boys and F. Bernardi, Molecular Physics **19**, 553–566 (1970).
[35]J. Hutson and S. Green, "Molscat computer code, version 14," Collaborative computational project (1994).
[36]A. M. Arthurs and A. Dalgarno, Proceedings of the Royal Society of London. Series A. Mathematical and Physical Sciences **256**, 540–551 (1960).
[37]S. Green, The Journal of Chemical Physics **62**, 2271–2277 (1975).
[38]M. H. Alexander and D. E. Manolopoulos, The Journal of chemical physics **86**, 2044–2050 (1987).
[39]T. Amano, K. Hashimoto, and T. Hirao, Journal of molecular structure **795**, 190–193 (2006).
[40]C. T. Bop, Y. Kalugina, and F. Lique, The Journal of Chemical Physics **156**, 204311 (2022).
[41]S. Demes, F. Lique, A. Faure, and F. F. van der Tak, Monthly Notices of the Royal Astronomical Society (2022), 10.1093/mnras/stac3221, stac3221, https://academic.oup.com/mnras/advance-article-pdf/doi/10.1093/mnras/stac3221/46909576/stac3221.pdf.
[42]M. Hernández Vera, F. Lique, F. Dumouchel, P. Hily-Blant, and A. Faure, Monthly Notices of the Royal Astronomical Society **468**, 1084–1091 (2017).

Appendix A: Anisotropy of the 4D PES with respect to ϕ

Fig. 8 displays the variation of the $HCNH^+-H_2$ 4D potential as a function of ϕ and R for selected values of θ_1 and θ_2. As mentioned in Sec. III, the anisotropy of the PES relative to ϕ is very low. For $\theta_1 = \{0°, 180°\}$, the interaction becomes completely isotropic. Indeed, $HCNH^+$ lies on the z-axis and the variation of ϕ changes only the x- and y-coordinates of the hydrogen atoms of H_2 but the interatomic distances remain the same and accordingly the PES. This is more obvious in the case where $\theta_2 = 90°$, i.e. the T-shape geometry of the complex.

Accepted to J. Chem. Phys. 10.1063/5.0141851

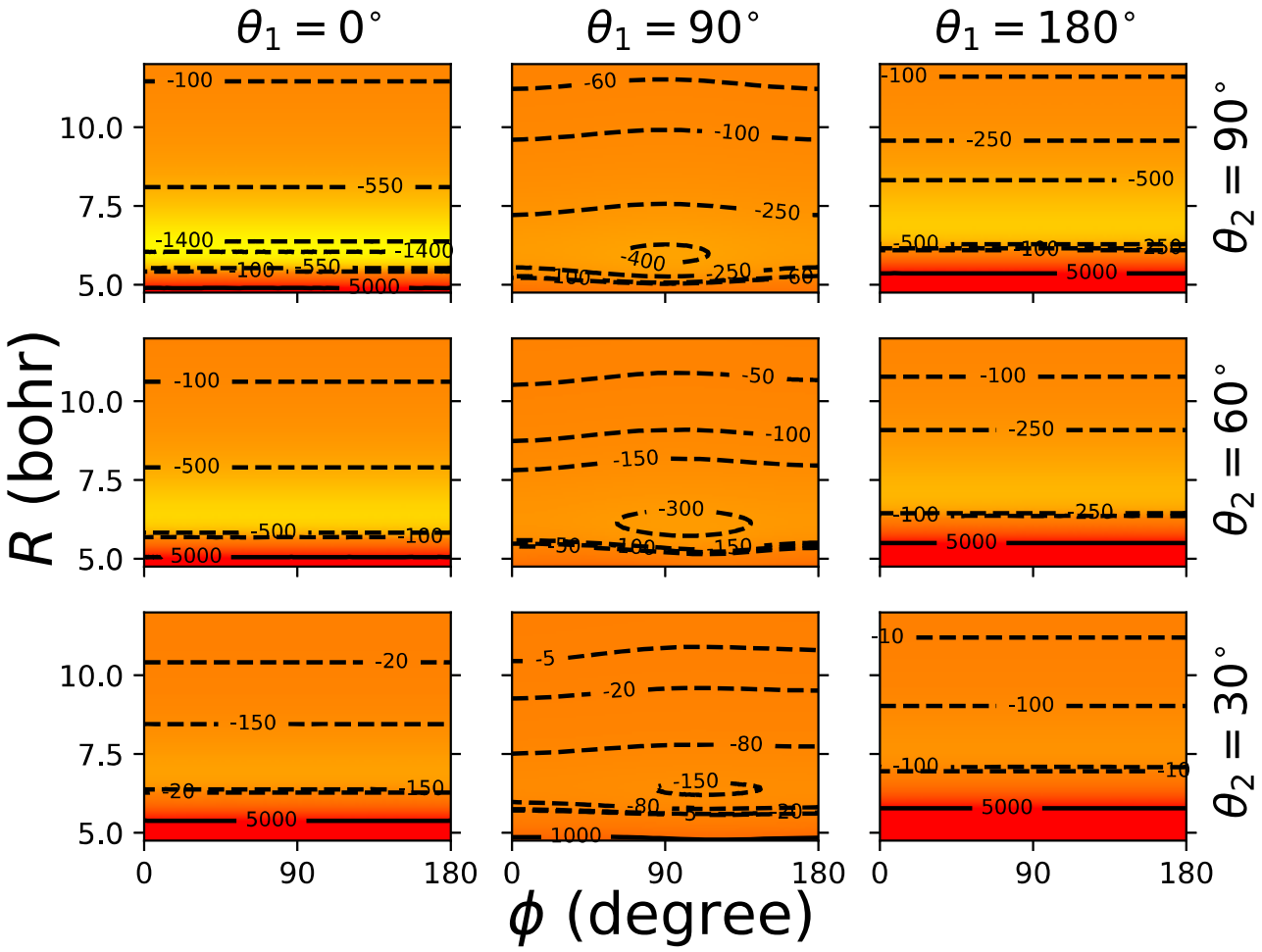

FIG. 8. Contour plots of the $HCNH^+-H_2$ interaction potential (in cm^{-1}) as a function of ϕ and R for selected values of θ_1 and θ_2.

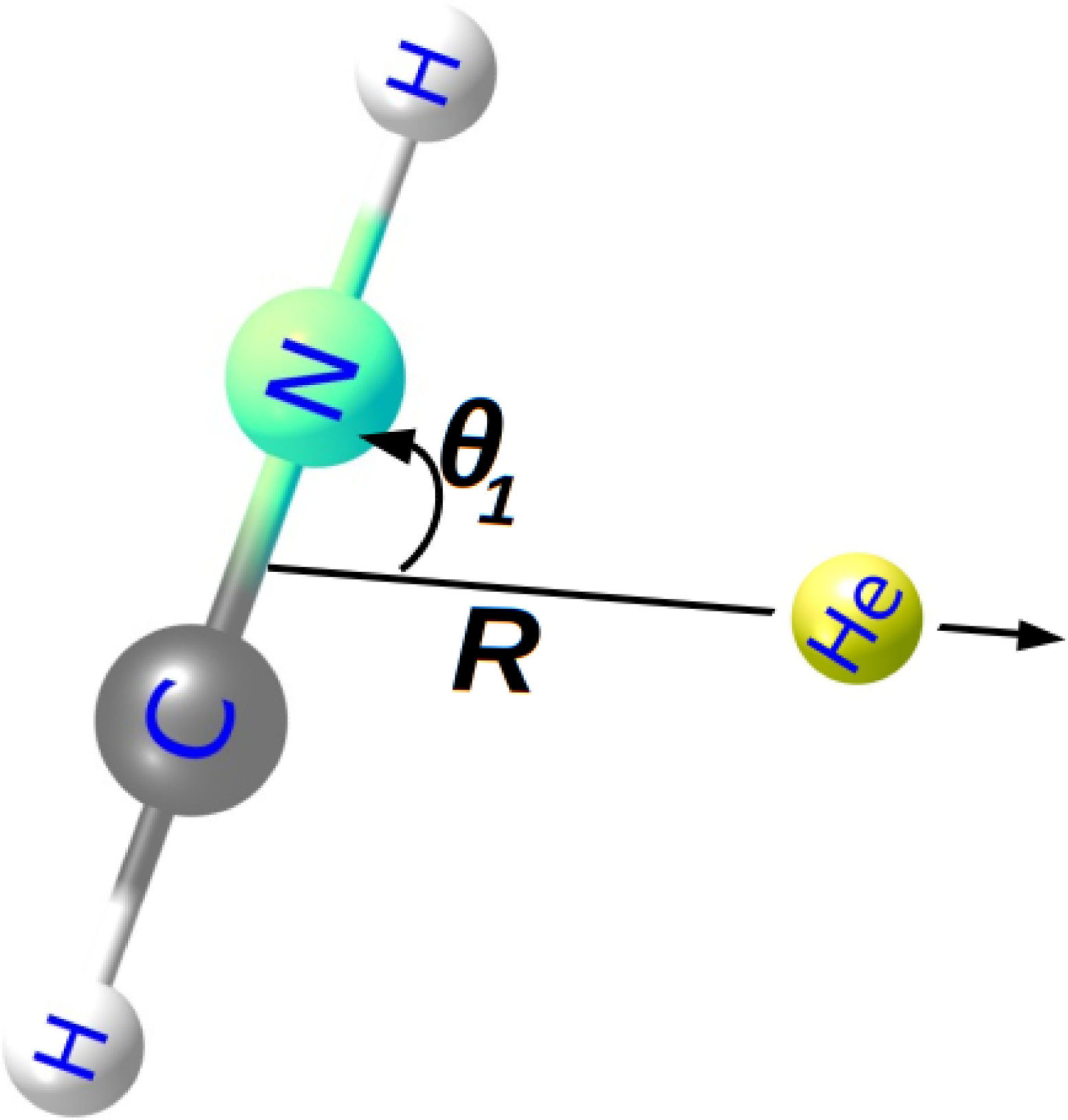
H
N
θ1
R
He
C
H

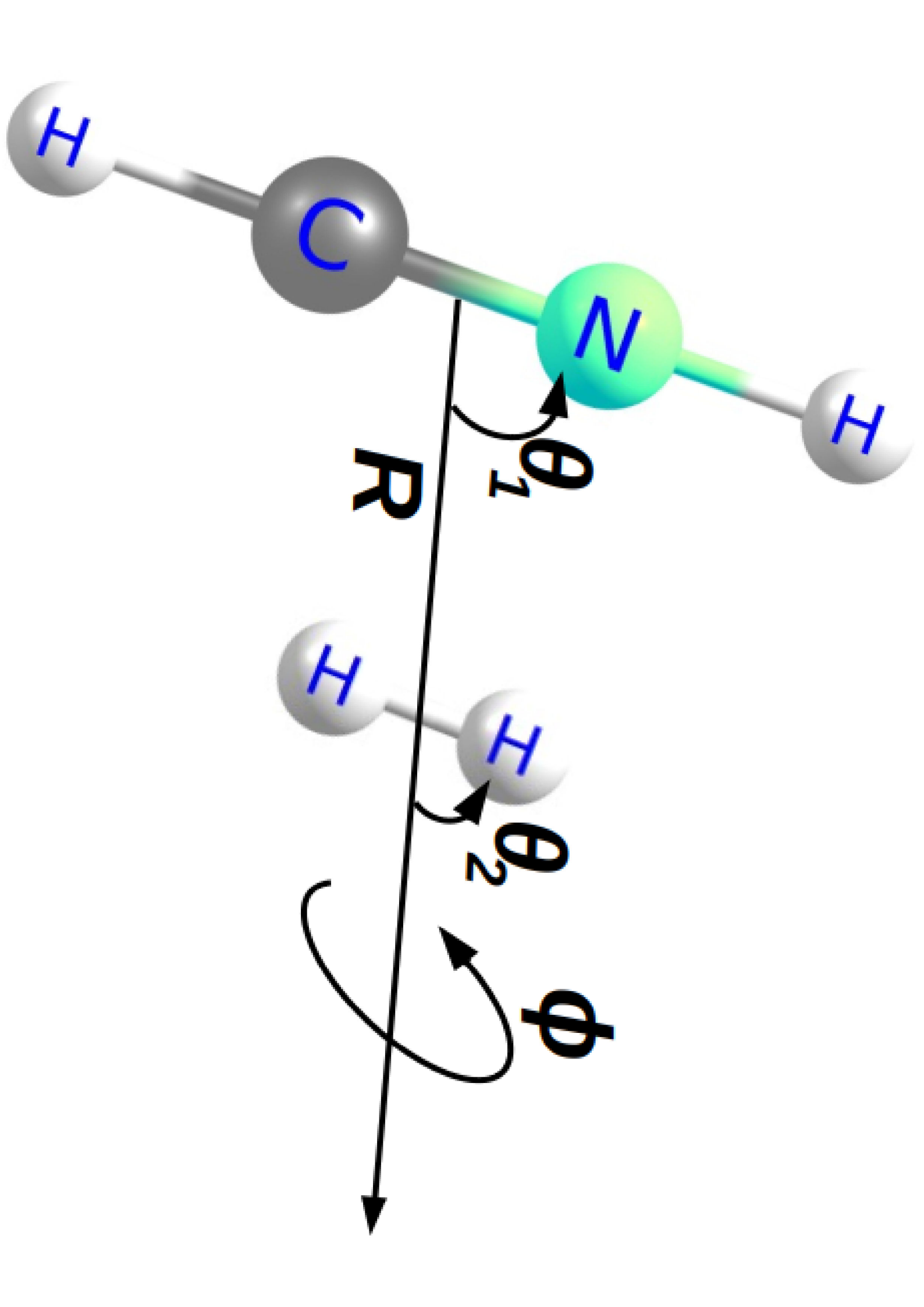
H
C
N
H
R
θ1
H
H
θ2
ϕ

Accepted to J. Chem. Phys. 10.1063/5.0141851

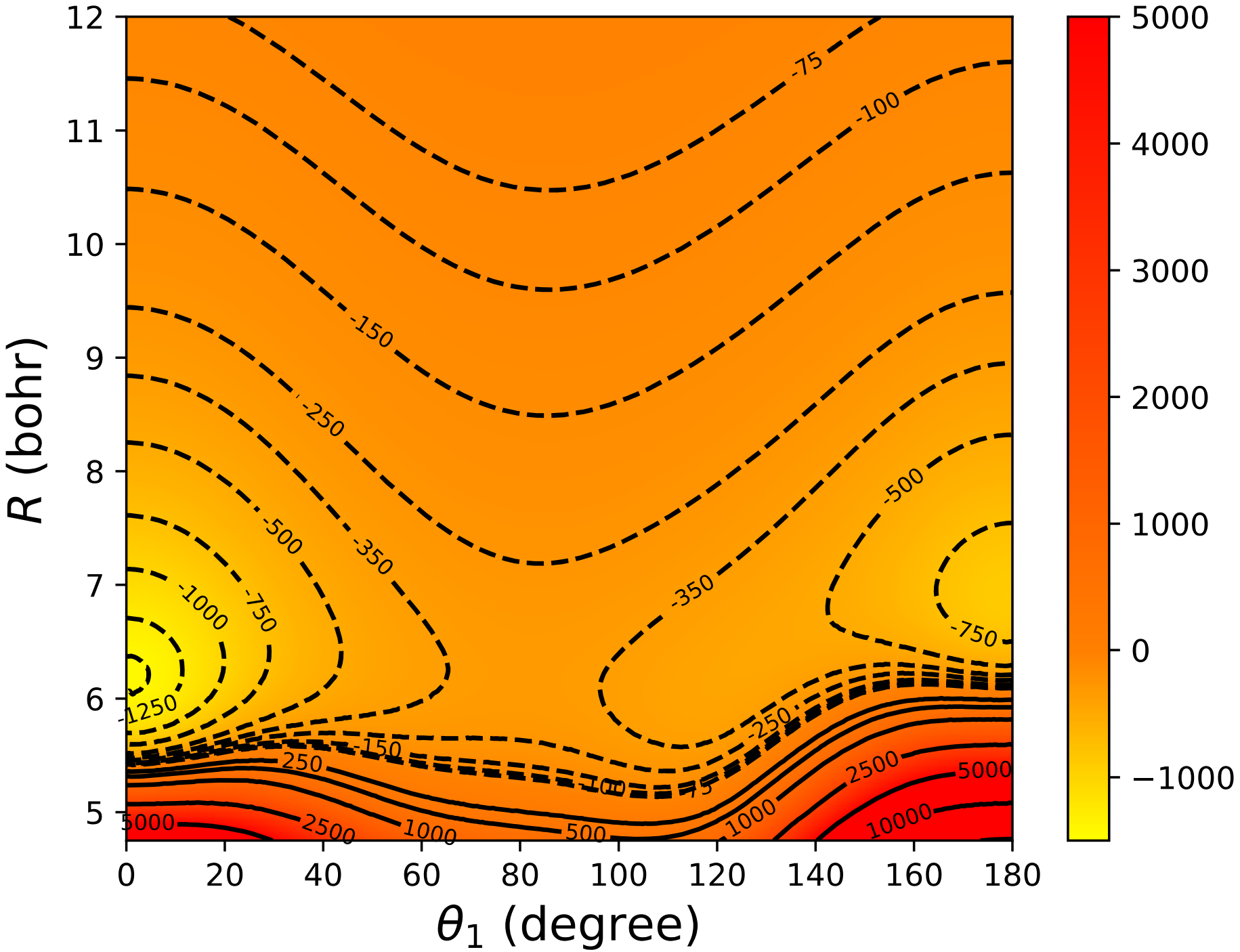

Accepted to J. Chem. Phys. 10.1063/5.0141851

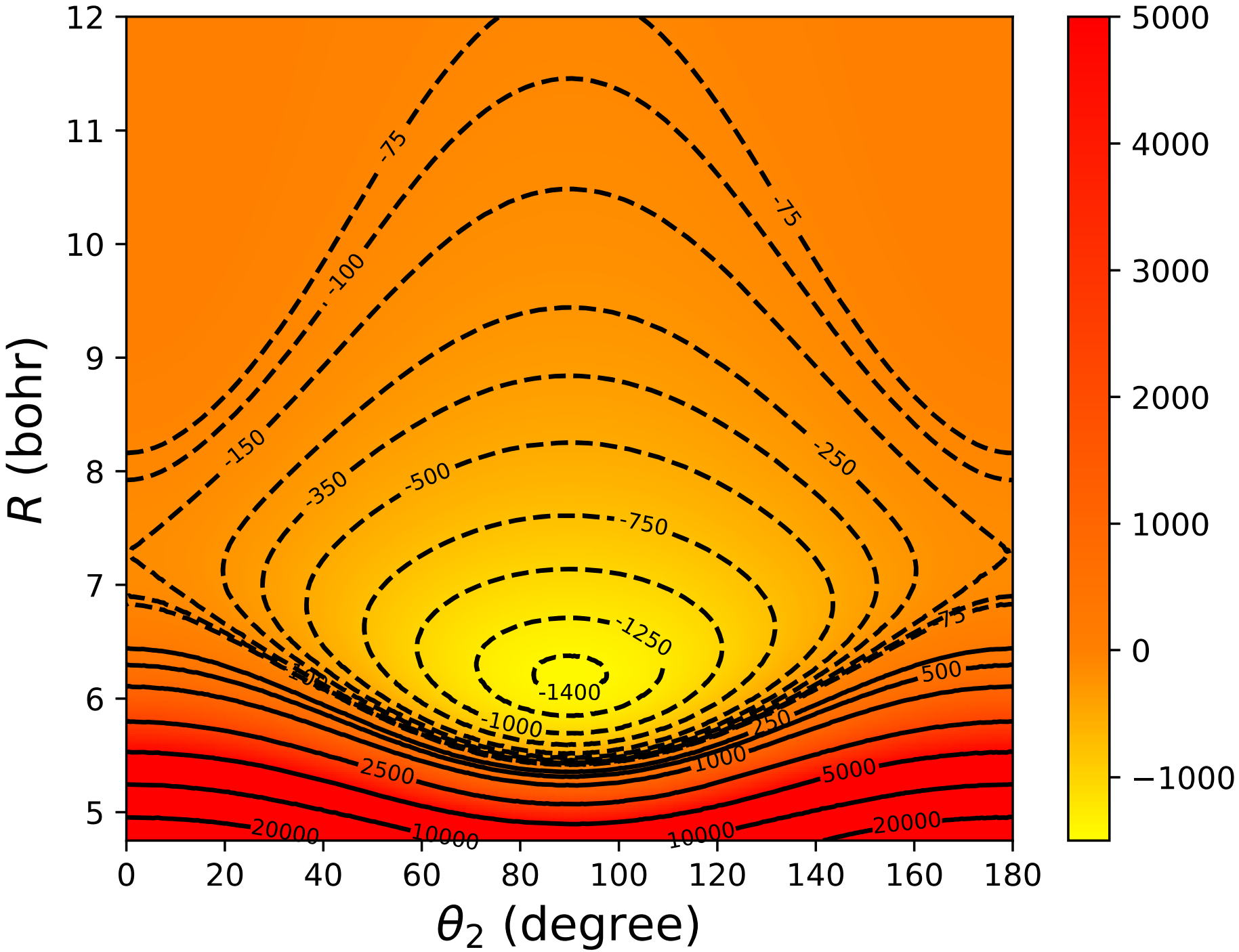

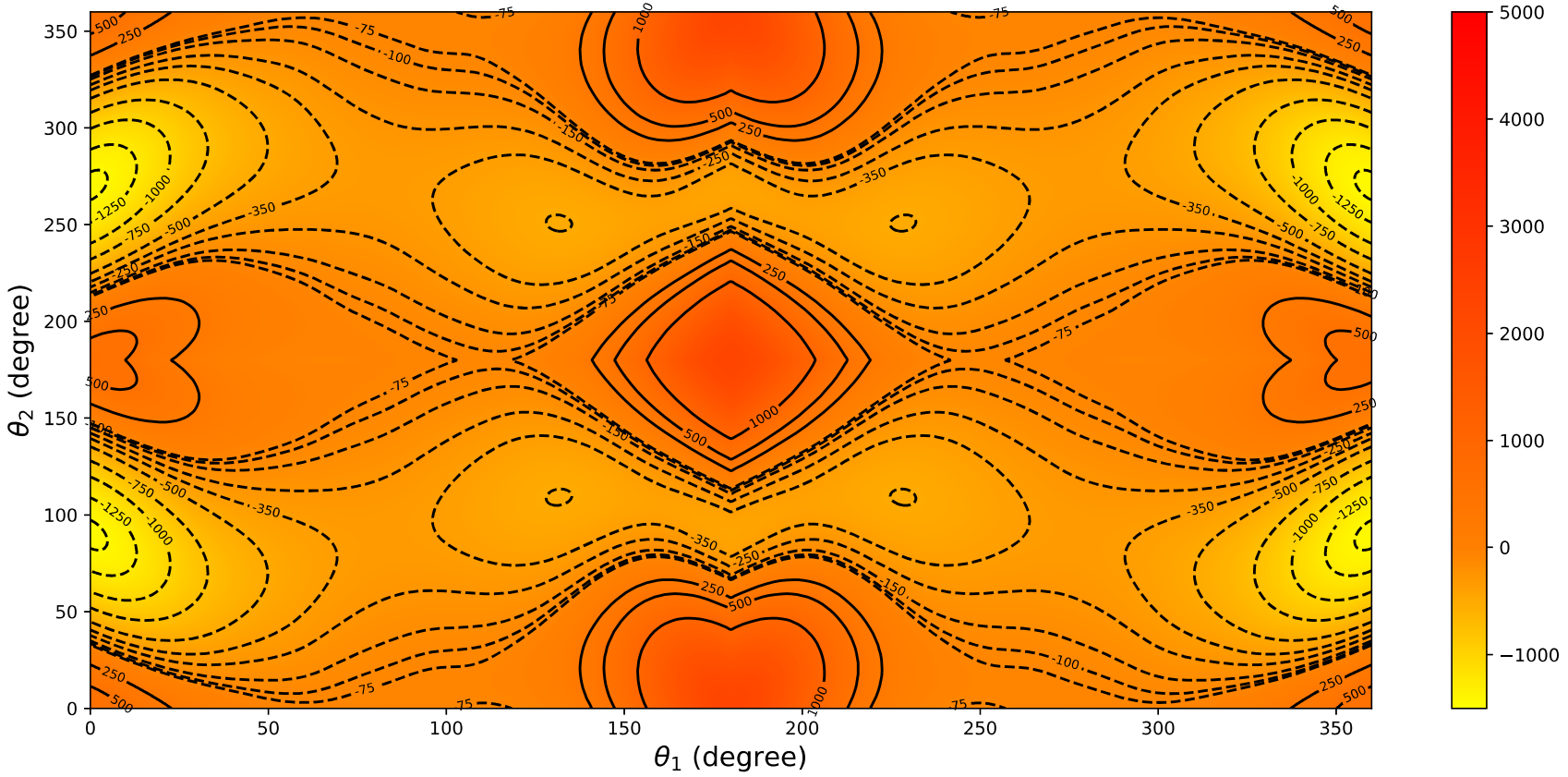

Accepted to J. Chem. Phys. 10.1063/5.0141851

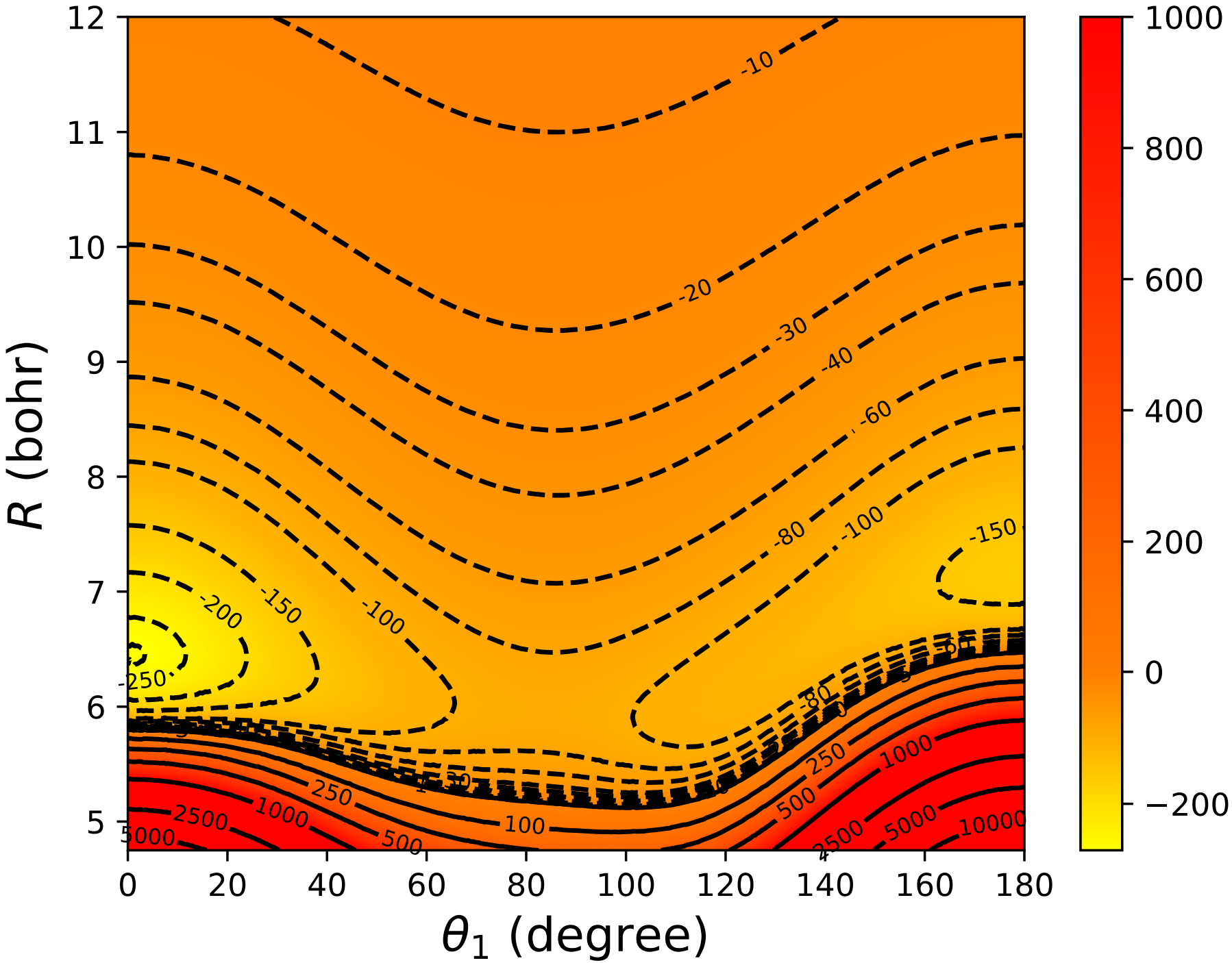

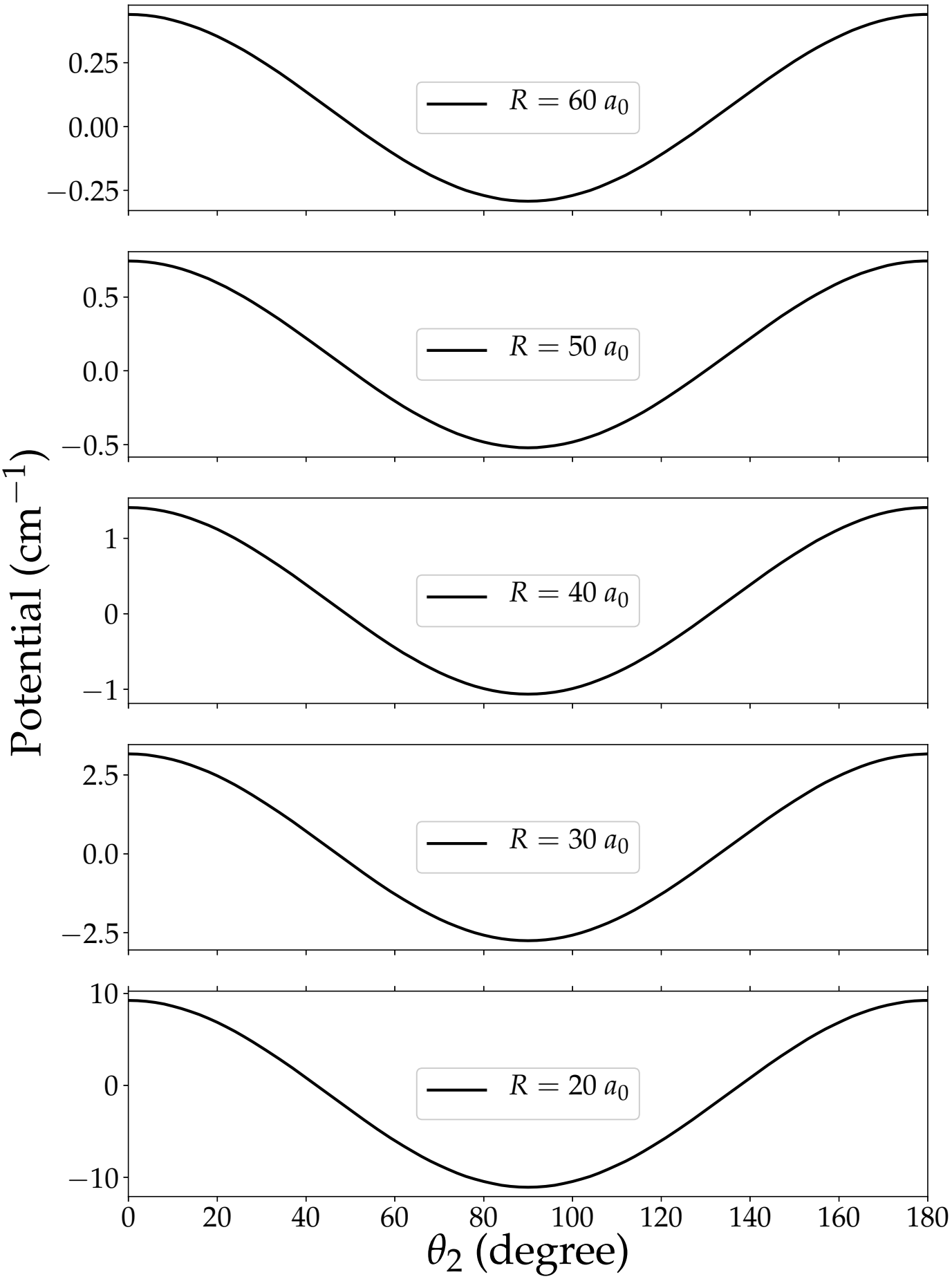
0.25
0.00
−0.25
$R = 60\ a_0$
0.5
0.0
−0.5
$R = 50\ a_0$
1
0
−1
$R = 40\ a_0$
2.5
0.0
−2.5
$R = 30\ a_0$
10
0
−10
$R = 20\ a_0$
Potential (cm^{-1})
0
20
40
60
80
100
120
140
160
180
θ_2 (degree)

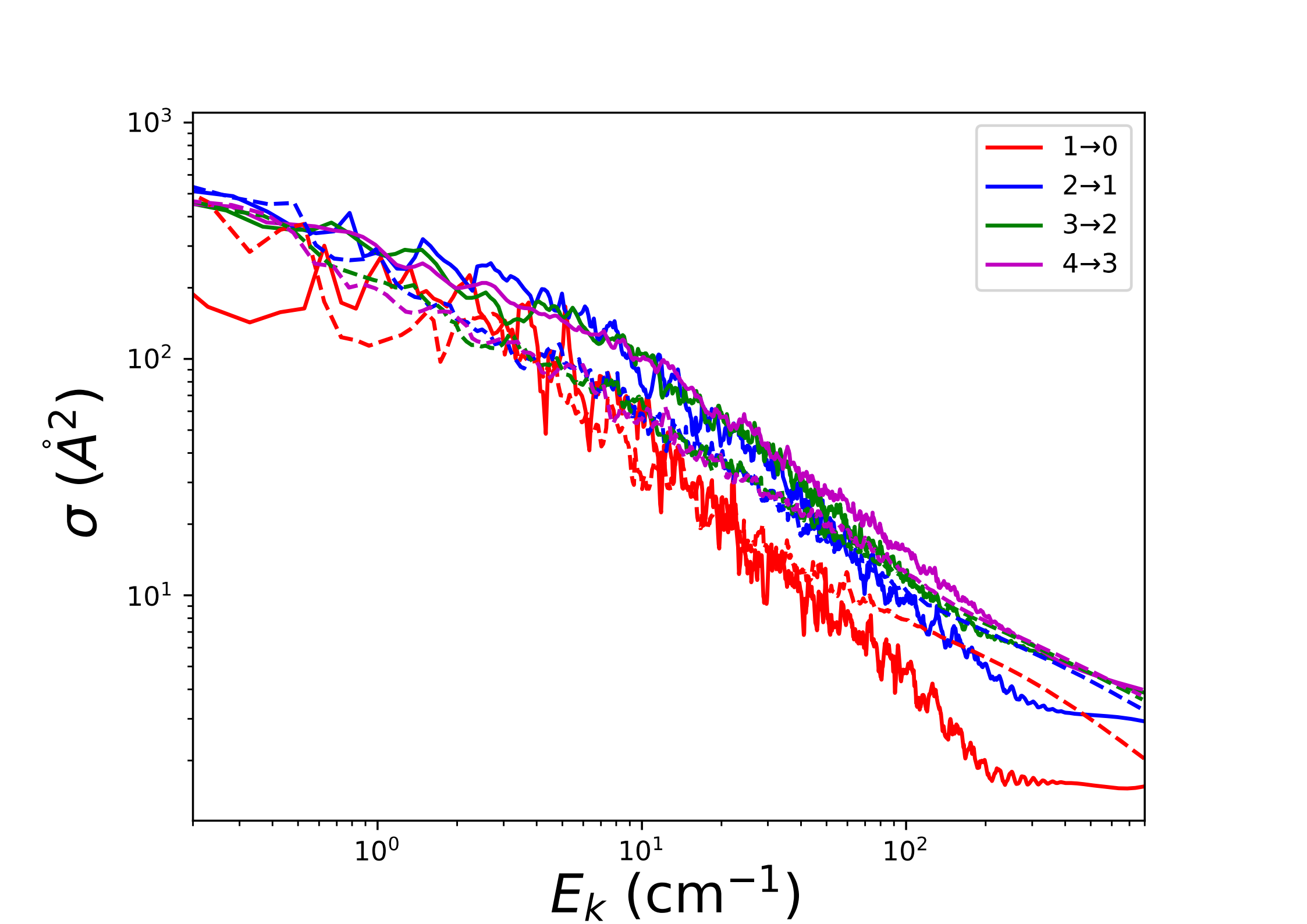
10^3
10^2
10^1
σ ($\mathring{A}^2$)
10^0
10^1
10^2
E_k (cm^{-1})
1→0
2→1
3→2
4→3

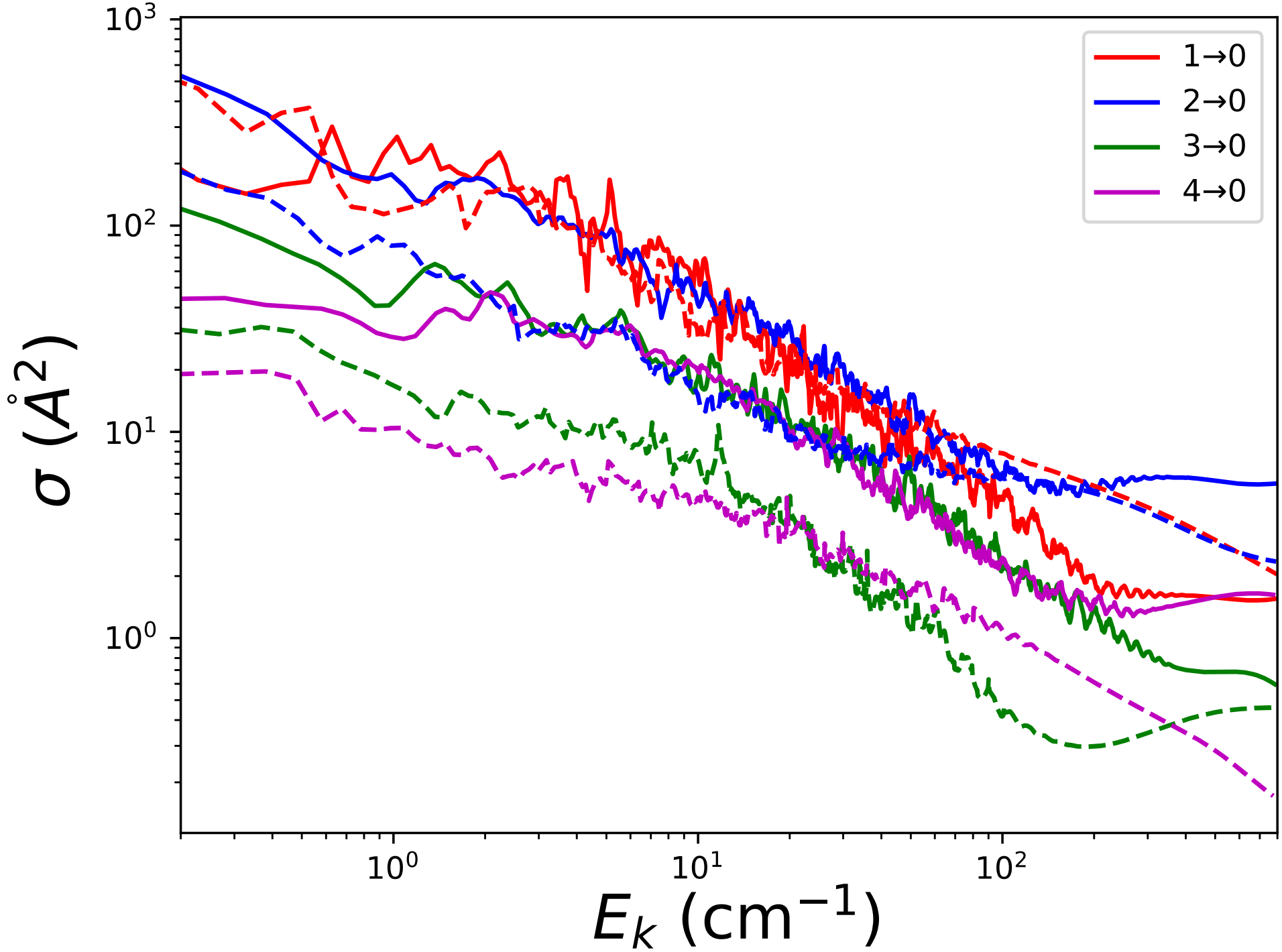
10^3
10^2
10^1
10^0
σ ($\mathring{A}^2$)
10^0
10^1
10^2
E_k (cm^{-1})
1→0
2→0
3→0
4→0

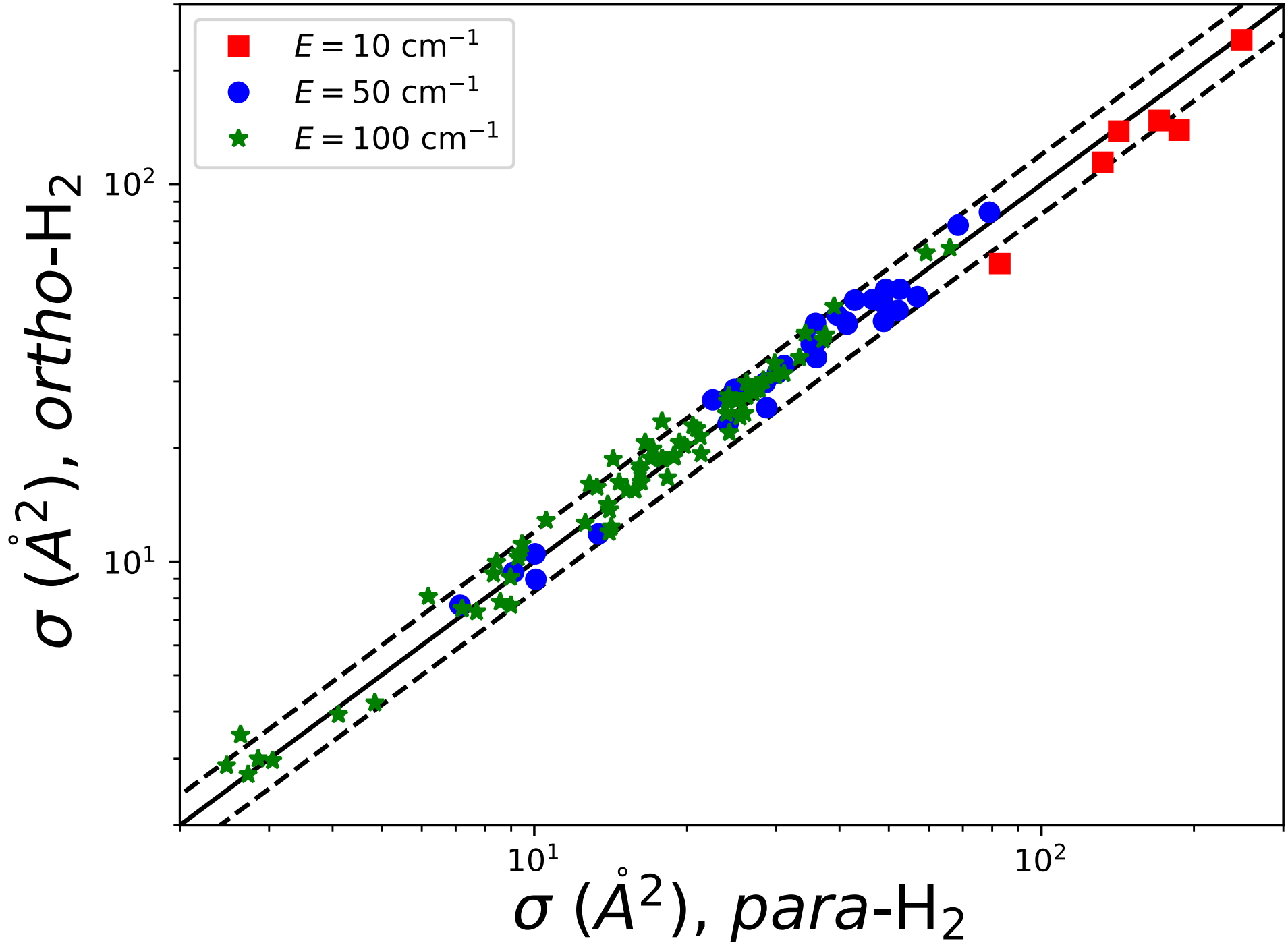
$E = 10\ \mathrm{cm}^{-1}$
$E = 50\ \mathrm{cm}^{-1}$
$E = 100\ \mathrm{cm}^{-1}$
10^2
10^1
10^1
10^2
$\sigma\ (\mathring{A}^2)$, *ortho*-H_2
$\sigma\ (\mathring{A}^2)$, *para*-H_2

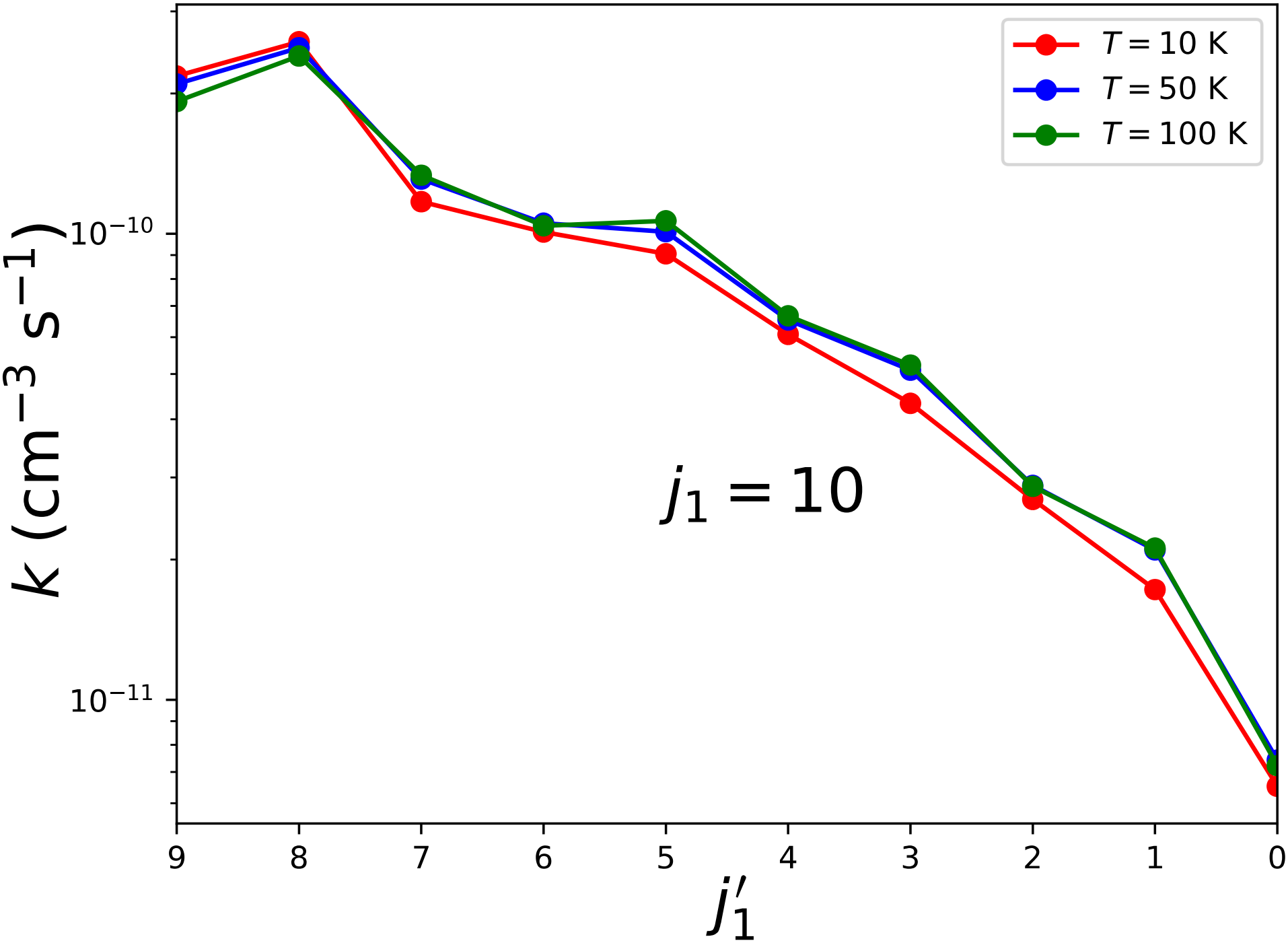
$T = 10$ K
$T = 50$ K
$T = 100$ K
$j_1 = 10$
k (cm^{-3} s^{-1})
10^{-10}
10^{-11}
9
8
7
6
5
4
3
2
1
0
j_1'

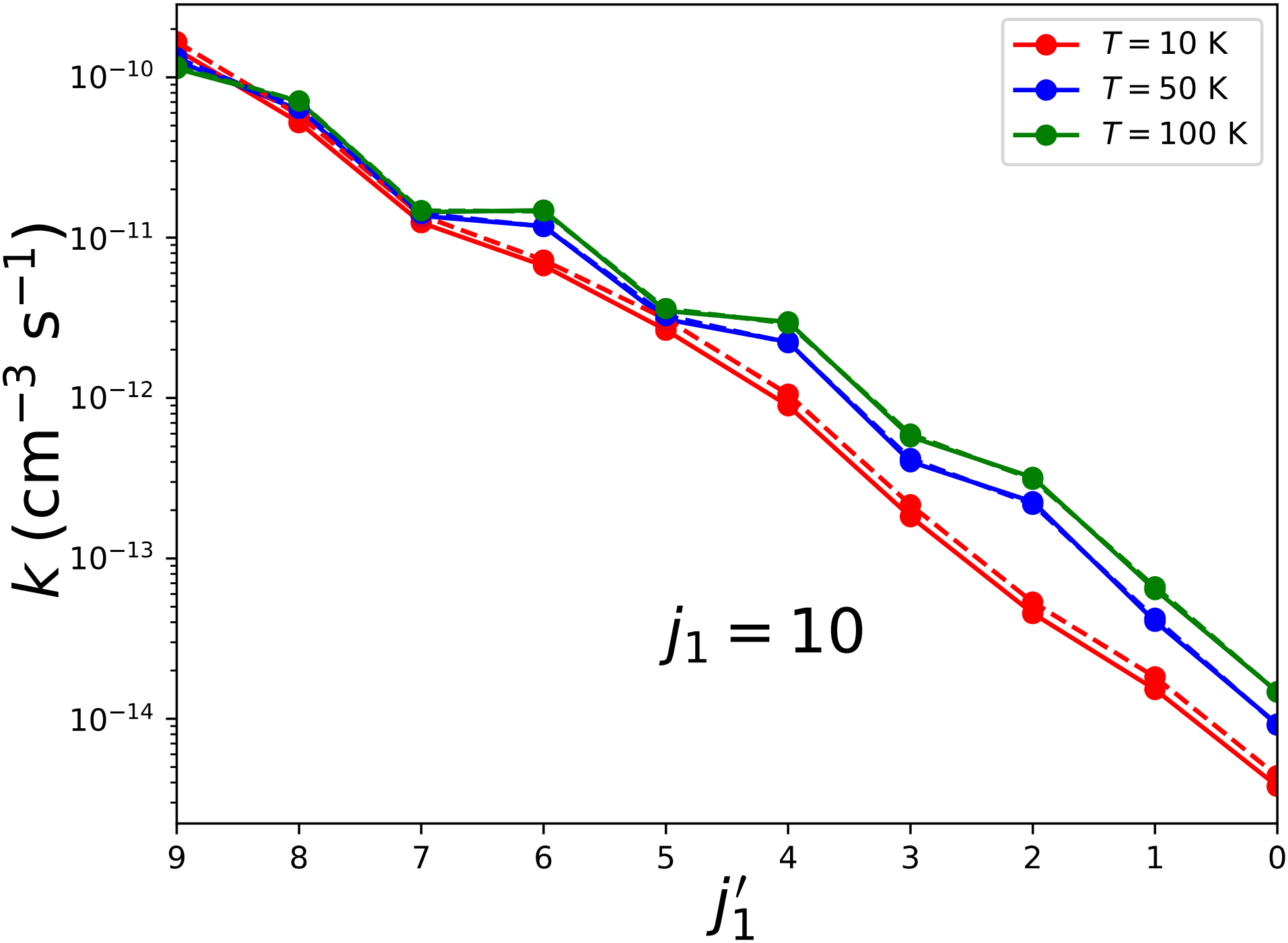
$T = 10$ K
$T = 50$ K
$T = 100$ K
$j_1 = 10$
k (cm^{-3} s^{-1})
10^{-10}
10^{-11}
10^{-12}
10^{-13}
10^{-14}
9
8
7
6
5
4
3
2
1
0
j_1'

Accepted to J. Chem. Phys. 10.1063/5.0141851